Advanced Sensor Research

ADVANCED SENSOR RESEARCH Open Access

www.advsensorres.com

RESEARCH ARTICLE OPEN ACCESS

Wireless and Soft Pulse Wave Measurement Device with Printed Ferroelectric E-tattoo Sensor

Karem Lozano Montero[1] | Yayun Du[2] | Ninja Kajas[1] | Jacob Trueb[2] | Mikko Peltokangas[3] | Hany Arafa[2] | Jin-Tae Kim[4] | Jianyu Gu[2] | Remmi Calvo Guzman[1] | Niku Oksala[3,5] | Jiantong Li[6] | Antti Vehkaoja[3] | John A. Rogers[2] | Matti Mäntysalo[1] | Mika-Matti Laurila[1,2]

[1]Faculty of Information Technology and Communication Sciences, Tampere University, Tampere, Finland | [2]Querrey Simpson Institute for Bioelectronics, Northwestern University, Evanston, Illinois, USA | [3]Faculty of Medicine and Health Technology, Tampere University, Tampere, Finland | [4]Department of Mechanical Engineering, POSTECH, Pohang, Republic of Korea | [5]Centre For Vascular Surgery and Interventional Radiology, Wellbeing Services County of Pirkanmaa, Tampere, Finland | [6]Division of Electronics and Embedded Systems, KTH Royal Institute of Technology, Kista, Sweden

Correspondence: Karem Lozano Montero (karem.lozanomontero@tuni.fi)

Received: 18 September 2025 | **Revised:** 13 February 2026 | **Accepted:** 20 February 2026

Keywords: arterial pulse wave measurement | biomedical devices | electronic tattoo sensor | ferroelectric devices | soft electronics

ABSTRACT

We propose a non-invasive pulse wave monitoring system that integrates a fully printed, partially stretchable ferroelectric electronic tattoo (e-tattoo) sensor with a soft, elastomer-encapsulated, partially stretchable data transmission unit (DTU). The DTU includes a rechargeable battery, Bluetooth-enabled wireless data transmission, and optimized signal conditioning circuitry for the e-tattoo sensor. We demonstrate: 1) a simple, printing-based fabrication process for the e-tattoo sensor and its integration with the DTU; 2) significant improvement in pulse wave index accuracy through optimized electrode material selection used in the e-tattoo sensor (e.g., reduction in relative error of relative crest time index from 56.3% to 0.2%); 3) enhanced sensitivity via integration of the e-tattoo on the DTU's soft encapsulation (increased from 25 pC/N to 1277 pC/N); and 4) successful extraction of clinically relevant pulse indices from radial artery of a human study subject.

1 | Introduction

Continuous monitoring of arterial pulse waves may be used for early detection of cardiovascular diseases (CVDs), which are among the leading causes of death worldwide, and for monitoring patients during and after CV-interventions. Ultra-thin (thickness < 10 μm) ferroelectric electronic tattoo (e-tattoo) sensors, which utilize the piezoelectric effect of ferroelectric materials for sensing, have been recently proposed to enhance user comfort in non-invasive detection and monitoring of CVDs via measurement of arterial pulse wave through skin deformation caused by the pulsating radial or carotid artery located directly underneath the skin [1–7]. In pulse-wave measurement, the ferroelectric e-tattoo sensor may be placed on top of the artery as a freestanding film [5, 7] or, e.g., using temporary tattoo adhesive [2]. The ultra-thin form factor of the e-tattoo sensor allows for increased deformation of the ferroelectric layer during arterial pulsation, thereby leading to higher sensitivity [1–7], increased signal-to-noise ratio, and, ultimately, more accurate pulse wave signal quality and CVD detection. Unlike conventional wearable devices, which can be bulky or less sensitive to subtle physiological changes, e-tattoos offer conformal contact with the skin and improved mechanical-electrical coupling, making them ideal for unobtrusive and sensitive monitoring.

Lithographic patterning followed by transfer printing on a flexible substrate (e.g., polyimide) has previously been used for the fabrication of e-tattoo sensors [5, 7–9]. However, print-

Karem Lozano Montero, Yayun Du, and Ninja Kajas. contributed equally to this work.

ing based fabrication [2, 3, 6] methods hold promise due to reduced number of process steps and compatibility with low temperature, solution-based functional materials, e.g., ferroelectric polymer poly(vinylidene fluoride-co-trifluoroethylene) (P(VDF-TrFE)) for ferroelectric layer and conductive polymer poly(3,4-ethylenedioxythiophene) polystyrene sulfonate (PEDOT:PSS) for conductors, thereby enabling device fabrication directly on, low heat budget substrates such as temporary tattoo paper.

However, regardless of the fabrication method, the e-tattoo sensor is often the only component that can be fabricated in an ultra-thin form factor, while other components of the measurement system (e.g., amplifiers for signal conditioning, energy source, wireless transmission circuitry) need to be fabricated with traditional components. In other words, the unobtrusiveness of e-tattoo-based pulse-wave measurement, is limited by the other components of the system. To this end, simpler systems for signal conditioning and wireless transmission have been proposed that operate using, e.g., near field communication [10] and surface acoustic wave devices [11, 12]. However, these devices pose a challenge, as they require an external device for radio-frequency power transmission, which must maintain a relatively unobstructed line of sight with the sensor to function properly. A solution is therefore needed that enables more robust data transmission, i.e., one not dependent on the immediate presence of an external device, while also leveraging the increased sensitivity and cost-effectiveness of printed e-tattoo-based ferroelectric sensors.

To this end, we propose a wireless and soft pulse wave measurement device with an integrated printed ferroelectric e-tattoo sensor. The device comprises a soft elastomer encapsulated and partially stretchable data transmission unit (DTU) with a rechargeable battery, Bluetooth wireless data transmission, and signal conditioning for a ferroelectric e-tattoo sensor, and a partially stretchable, fully printed ferroelectric e-tattoo sensor integrated on the outer surface of the DTU. We demonstrate a simple, printing-based fabrication of the e-tattoo sensor directly on temporary tattoo paper and its facile integration with the DTU. Moreover, we show that the accuracy of clinically relevant pulse wave indices obtained with the e-tattoo sensor can be significantly improved by controlling the leakage current of the e-tattoo sensor via optimization of the electrode material, and we also demonstrate that the system can utilize the high sensitivity of the e-tattoo sensor via soft elastomer-based sensitivity amplification. Finally, we show that the system can be used to obtain clinically relevant pulse wave indices from the radial artery of a human study subject. These results pave the way toward an unobtrusive, affordable, and accurate bio-signal measurement system for continuous, large-scale screening of populations at risk for CVDs and for monitoring of patients during and after interventions.

2 | Experimental Section

2.1 | Fabrication of Ultra-Thin Ferroelectric E-Tattoo Sensors

For sensor optimization experiment (Section 3.1), ultra-thin ferroelectric e-tattoo sensors were fabricated on temporary tattoo paper using the following steps (detailed process parameters and materials in Section S1): 1) removal of the water-soluble layer from the tattoo paper, 2) inkjet printing of the bottom electrode, 3) curing of the bottom electrode, 4) deposition of P(VDF-TrFE) using a motorized film applicator, 5) curing of the P(VDF-TrFe) layer, 6) inkjet printing of the top electrode using cross-linked PEDOT:PSS (see below) 7) curing of the top electrode, and 8) in situ poling of P(VDF-TrFE). Three different bottom electrode materials were used in step 2: pristine PEDOT:PSS, cross-linked PEDOT:PSS, and silver nanoparticle ink. After completing the fabrication steps, temporary tattoo adhesive (Silhouette Studio) was applied to the top side of the e-tattoo sensor, which was then adhered to the mock circulatory loop system designed to mimic the human heart. The backing paper was released by soaking in DI water.

For sensor-to-DTU integration (Section 3.2) and pulse wave measurement (Section 3.4) fabrication followed the same procedure using cross-linked PEDOT:PSS as the bottom electrode material, with additional steps: 9) inkjet printing of stretchable PEDOT:PSS interconnects, 10) curing of the stretchable interconnects, 11) deposition of a PDMS layer with a motorized film applicator, 12) curing of the PDMS layer, 13) formation of a stress-release pattern/layer by cutting through the PDMS and e-tattoo sensor stack.

2.2 | Electrical, Ferro- and Piezoelectric Characterization

Dynamic hysteresis measurements were performed at a frequency of 2.5 Hz and an electric field of 90 V/μm using a ferroelectric tester (TF2000, AIXACCT) coupled with a high-voltage amplifier (610C, TREK) to obtain saturated polarization – electric field (PE) loops. Leakage current measurements were also conducted up to 1 V/μm using the same setup.

The direct piezoelectric coefficient (d_{33}) was measured with a piezotester (PM300, Piezotest Ltd.) by clamping the e-tattoo sensor (on temporary tattoo paper) between two convex probes under a static force of 10 N and then applying a sinusoidal mechanical excitation (0.25 N amplitude, 110 Hz). The capacitance at 1 kHz was also measured using the piezotester.

Bending-mode sensitivity was measured by transferring the e-tattoo sensor from the temporary tattoo paper onto the DTU, then clamping the combined assembly in the piezotester. Static (~100 mmHg) and dynamic (9.6–38.2 mmHg) pressures were applied to simulate typical diastolic and systolic pressure ranges. Three e-tattoo sensors were characterized, with five repeated measurements per dynamic pressure level.

2.3 | E-Tattoo Sensor and Charge Amplifier Bandwidth Optimization

The sensor and charge amplifier bandwidths were optimized using a mock circulatory loop (MCL) system. The system comprises two cylinders representing the right atrium (RA) and right ventricle (RV), along with two prosthetic heart valves simulating the pulmonary valve (PV) and tricuspid valve (TV). It incorporates a commercial flow sensor (TS410 tubing module, Transonic Systems Inc.) and a pressure sensor (Tru-Wave Disposable Pressure Transducer, Edward Lifesciences). One of the cylinders,

equipped with a mechanical pump that replicates the contraction of the RV, drives flow into the pulmonary artery (PA) through a bi-leaflet mechanical valve, emulating the function of the PV. The flow then passes through the commercial sensors and into the second cylinder, which is connected to a temperature control module set to 37°C and a caged ball valve representing the RA and TV, respectively. A PC with a custom graphical user interface (GUI) receives inputs to control the pump's frequency and amplitude, generating the oscillatory flow waveform and displaying real-time flow and pressure data collected by commercial sensors.

The charge amplifier bandwidth optimization was conducted using MCL (Section S2 and Figure S1a) to generate a pulse wave. This pulse wave was simultaneously recorded by the pressure sensor (reference sensor) of the MCL and an ultra-thin printed P(VDF-TrFE) ferroelectric e-tattoo sensor with an Ag bottom electrode and a measured low cutoff frequency of ~3mHz. The e-tattoo was attached to an elastic pipe downstream of the commercial flow sensor (Section 2 and Figure S1b), and it therefore measured the pipe deformation. The e-tattoo ferroelectric sensor output was amplified using a prototype charge amplifier implemented with an AD8531 operational amplifier with a 2 GΩ feedback resistor. The low cutoff frequency of the amplifier was varied by varying the value of the feedback capacitor ($f_{low} = 1/(2*\pi*R*C)$). The best correspondence was obtained with a 1500 pF capacitor, resulting in $f_{low} = 53$ mHz (Section S2 and Table S2).

For the e-tattoo sensor bandwidth optimization, the above measurement setup was used with the optimized charge amplifier and three different bottom electrode samples (Ag, cross-linked PEDOT:PSS, pristine PEDOT:PSS) with varying low cutoff frequency were attached to the elastic pipe downstream of the commercial flow sensor.

2.4 | Data Transmission Unit (DTU)

An exploded view of the proposed wireless and soft pulse wave measurement device, shown in Figure 1a, illustrates the main components and structural layout of the DTU. At the core of the DTU is a system-in-package (SiP) module, the ISP1807 (InsightSIP), a compact Bluetooth Low Energy (BLE) module that integrates a powerful processor capable of supporting complex applications. It is compliant with the full Bluetooth 5.0 specification and includes an onboard antenna and RF matching circuitry.

The DTU is wirelessly rechargeable via an integrated wireless charging coil system, coupled with the nPM1100 power management integrated circuit (Nordic Semiconductor). This unit regulates the charging current and manages power delivery to the system. Configured with external resistors, the nPM1100 steps down the LiPo battery voltage (3.3–4.2 V) to a stable 1.8 V output, which powers the primary components, including the ISP1807, a 2 Gbit non-volatile memory (W25N02KWZEIR, Winbond Electronics), and an inertial measurement unit (IMU) (LSM6DSO32TR, STMicroelectronics).

Signal conversion is handled by a transimpedance amplifier (TIA) circuit utilizing an operational amplifier (AD8531ARZ, Analog Devices Inc.), operating at 3.3 V. This voltage is provided by a linear voltage regulator (ADP7112ACBZ-3.3-R7, Analog Devices Inc.), which delivers clean power to sensitive analog circuitry. The TIA converts the sensor's output current into a measurable voltage. As detailed in Section S2 (Figure S1c and Table S2), the feedback resistor and capacitor are set to 2 GΩ and 1500 pF, respectively, resulting in a low cutoff frequency of approximately 53 mHz.

The DTU's interconnects employ a serpentine geometry designed to enhance mechanical durability and accommodate stretching, enabling conformal integration with wrists of varying sizes. This structural design ensures both flexibility and reliable electrical performance under deformation. To ensure operational safety and extend battery lifespan, thermal protection is implemented via a negative temperature coefficient (NTC) thermistor. Charging is automatically halted, and the load is disconnected if the temperature falls outside the safe operating range.

To enable real-time battery level monitoring and intelligent power switching, a complementary ChipFET (NTHC5513T1G, onsemi) is used. This dual MOSFET package includes both N-channel and P-channel devices, facilitating efficient battery status management and load switching.

2.5 | E-Tattoo Sensor to DTU Integration

First, the adhesion of the DTU silicone elastomer encapsulation and the stress release layer of the e-tattoo sensor to the temporary tattoo adhesive was improved by treating the DTU with UV-ozone, and the top side of the e-tattoo sensor and temporary tattoo adhesive with RF-plasma (see detailed process parameters in Section S1). This was followed by attaching the temporary tattoo adhesive to the top side of the e-tattoo sensor, attaching ECG-gel to the PCB-to-sensor connection pads to form a soft electrical connection, adhering the e-tattoo sensor to the DTU (as shown in Figure 1), and releasing the temporary tattoo backing paper by soaking it in DI water. Finally, a protective stretchable film was attached on top of the integrated e-tattoo sensor.

2.6 | Mechanical Testing

To simulate the stretching forces that occur when the DTU is attached to a wrist, a dummy e-tattoo sensor (with electrodes shorted through the P(VDF-TrFE)) was integrated into the DTU, and the change in the resistance was measured using an electrometer while bending the DTU using a motorized tension/compression stand (ESM303, Mark-10). The bending tests were performed such that the e-tattoo sensor was either on the concave side or the convex side of the bend. The movement distance was set to 10 mm, resulting in a maximum bending radius of approximately 10 mm. Approximately 30 bending cycles were performed. Additionally, to estimate the maximum stretchability of the printed serpentine interconnection, a printed connector was fabricated following fabrication steps 9–13 (Table S1). The sample was then attached to a soft elastomer using the same procedure as for the e-tattoo sensor. The elastomer carrying the connector was subsequently stretched uniaxially using a motorized tension/compression test stand (ESM303, Mark-10) (Figure S4).

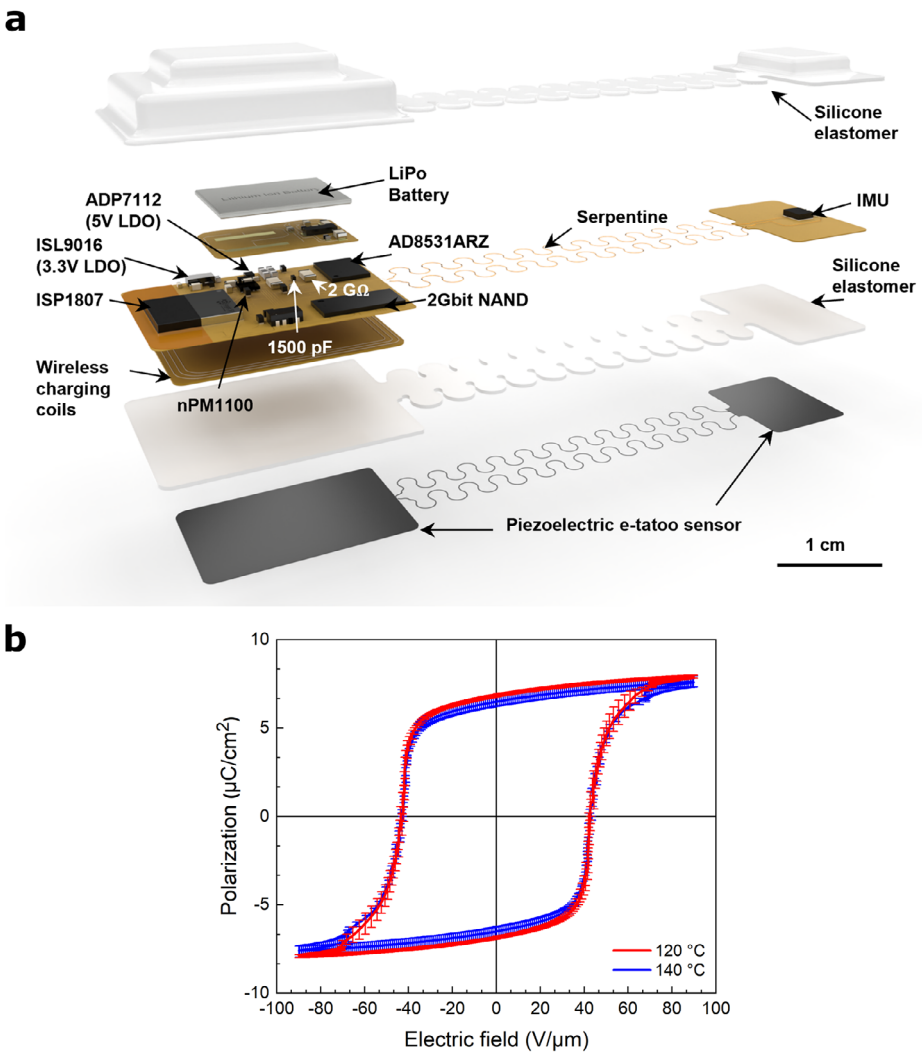

FIGURE 1 | a) An exploded view of the proposed wireless and soft pulse wave measurement device comprising the DTU and the ferroelectric/piezoelectric e-tattoo sensor, and b) Effect of curing temperature on polarization vs. electric field loop of P(VDF-TrFE) samples (n = 3). Range bars show the min and max polarization values for each data point.

TABLE 1 | Effect of curing temperature on remanent polarization, coercive field, and piezoelectric d_{33}-coefficient of P(VDF-TrFE).

T (^{0}C)	P_r (μC/cm^2)	d_{33} (pC/N)
120	6.8	28.8
140	6.5	24.2

2.7 | Pulse Wave Measurement

Arterial pulse wave measurement was conducted in the sitting position on a voluntary test subject, 36 years of age, with no previous history of cardiovascular diseases. Under the ethical guidelines of Tampere University, measurements conducted on a participating researcher (i.e., author of the manuscript) do not require ethical approval. The participating author provided informed consent to participate in the study. No identifiable personal information is disclosed in this manuscript. The DTU, along with the printed ferroelectric e-tattoo sensor, was attached to the skin on the top of the pulsating radial artery at the distal antebrachium of the left upper limb, and a snap-on wrist band was placed on top of the DTU to provide a biasing force (Section S5). The obtained pulse wave was recorded wirelessly on an iPad.

For pulse wave signal post-processing, a second-order Butterworth filter with a passband of 50 mHz to 7 Hz was applied to remove a certain amount of baseline wandering and all high-frequency noise (e.g., noise related to 50 Hz mains) from the obtained pulse wave signals. This was followed by detecting the individual pulses in the continuous pulse wave signal by first inverting the pulse wave signal and then separating the pulse wave signal into individual pulses based on data points detected by using a pre-determined peak prominence and peak-to-peak distance. A linear trend was then removed from the individual pulses based on the starting and ending points, followed by amplitude normalization of the individual pulses. An average pulse wave was then calculated based on the amplitude-normalized individual pulses, with 108 pulses included in the average. Finally, clinically relevant pulse wave indices (i.e., relative crest time, reflection index, relative dicrotic wave time, and stiffness index) were extracted from the average pulse wave.

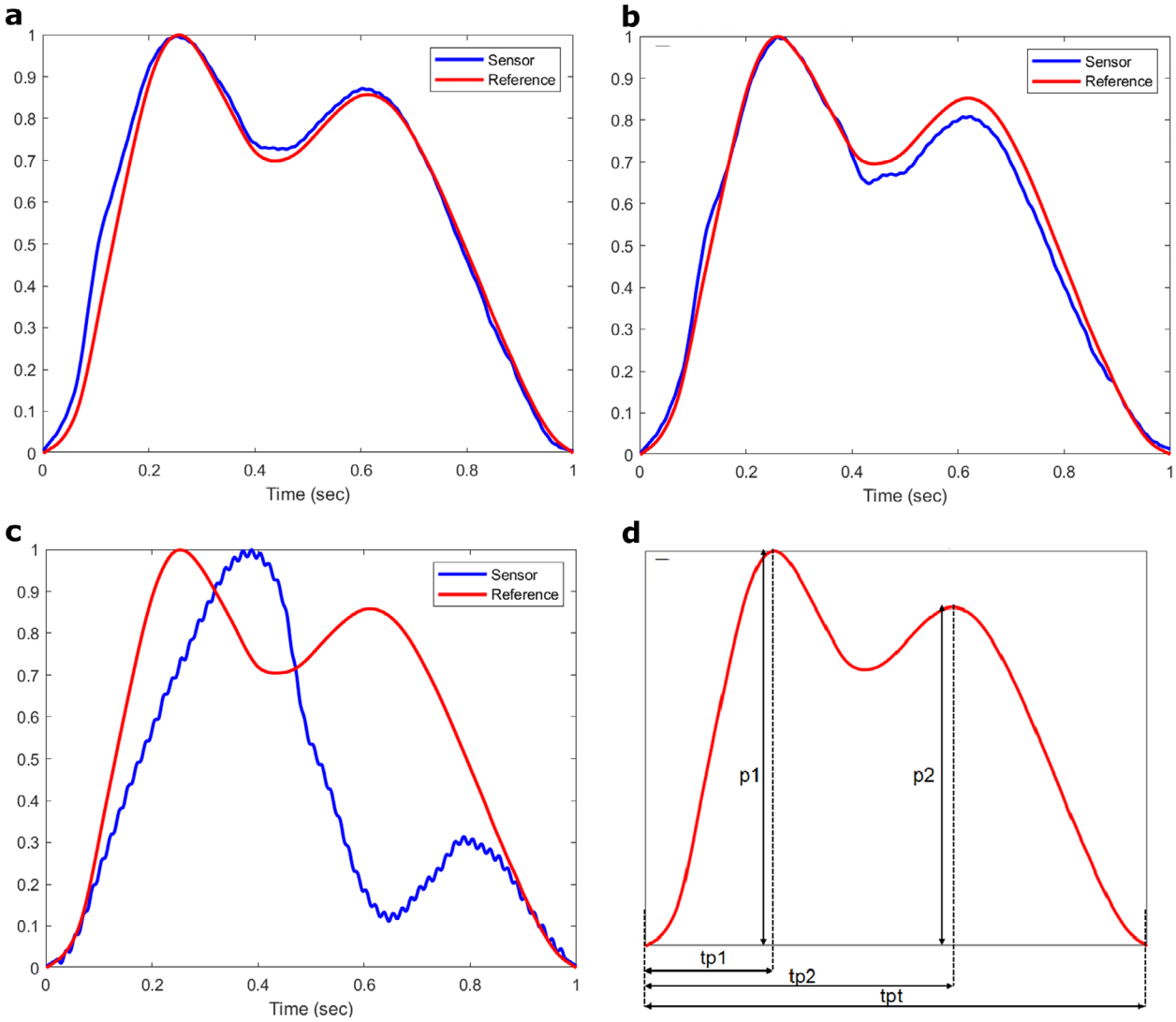

FIGURE 2 | Comparison of MCL generated reference pulse wave (red) and e-tattoo sensor obtained pulse waves (blue) at 60 BPM for: a) E-tattoo sensor with Ag bottom electrode, b) E-tattoo sensor with cross-linked PEDOT:PSS bottom electrode, and c) E-tattoo sensor with pristine PEDOT:PSS bottom electrode; d) Shows the fiducial points of the pulse wave used to calculate clinically relevant pulse wave indices.

2.8 | Statistical Analysis

All experimental data are presented as mean values unless otherwise stated. For d_{33} and bending mode sensitivity measurements, five measurement points were recorded per sample from three independently fabricated samples. Standard deviation (SD) is reported where specified (e.g., linear fits and selected bar graphs), while error bars represent either sd or minimum–maximum values as indicated in the respective figure captions. Statistical comparisons were performed using a paired sample t-test with significance defined as $p < 0.05$. curve fitting, statistical analysis, and data visualization were carried out using origin 2019

3 | Results and Discussion

3.1 | E-Tattoo Sensor Optimization

The optimization of the ferro- and piezoelectric performance of the ferroelectric P(VDF-TrFE) layer is crucial for maximizing the sensitivity of the e-tattoo sensor, which, in turn, affects the accuracy of the obtained pulse wave signal by increasing the signal-to-noise ratio. The ferro- and piezoelectric properties of P(VDF-TrFE) are impacted by the curing step, which promotes crystal growth and the formation of the polar β-phase [13], and the poling step, which promotes the homogenous reorientation of the permanent dipole moments of the β-phase crystals [14]. The optimal temperature for the curing step is close to the Curie temperature [13], which is around 136 ^{0}C for the 80:20 VDF: TrFE composition used in this study [15]. However, the sensor fabrication directly onto a temporary tattoo paper with a maximum processing temperature of around 120 ^{0}C limits the possibility to achieve the Curie temperature. To demonstrate that this limitation does not significantly impact the ferro- and piezoelectric properties of P(VDF-TrFE), average polarization-electric field loops (PE-loops) for three samples cured for 1 h at 120 ^{0}C and 140 ^{0}C are shown Figure 1b, and the average piezoelectric d_{33}-coefficients values for these samples are shown in Table 1, together with remanent polarization (P_r) values extracted from the PE-loops. Interestingly, no statistically significant difference

(based on paired sample t-test) was observed between the remanent polarization values, but the average d_{33}-coefficient of samples cured at 120°C was decreased by ~16% when compared to samples cured at 140°C. Although a positive correlation between the remanent polarization and piezoelectric coefficient is often observed, it is possible that the lower curing temperature leads to a smaller crystallite size, which has been observed to affect the d_{33}-coefficient, but not necessarily the remanent polarization [16]. Furthermore, it is possible that the lower curing temperature and smaller grain size increase the concentration of defects or residual stresses that pin domain walls, reducing their mobility during relatively small forces present during mechanical excitations. Since domain wall motion contributes significantly to the piezoelectric effect, restricted mobility can result in a lower d_{33}-coefficient. However, the strong electric field applied during the PE-loop measurement may be sufficient to overcome the residual stresses pinning the domain walls, which is why a similar reduction of ferroelectric performance is not observed. Nevertheless, the ~16% reduction in piezoelectric performance should be neglectable from the perspective of the S/N-ratio and pulse wave accuracy, especially as the sensor sensitivity is significantly increased when the e-tattoo sensor is attached to the DTU (see Section 3.3).

In addition to ferro- and piezoelectric performance, one of the main considerations when designing pulse wave sensors based on the piezoelectric transduction principle is the suitable bandwidth of the sensor. To have an accurate representation of the pulse wave signal, one needs to design a sensor (and sensing system) having a pass-band ranging from tens of mHz range up to around ten hertz [17, 18]. However, it is the low-frequency end of the spectrum that may pose challenges when designing ultra-thin ferroelectric sensors. This challenge results from the dependence of the low cutoff frequency (henceforth cutoff frequency) of the sensor on capacitance (C) and leakage current (i.e., leakage resistance R) of the ferroelectric layer, according to $f_{low} = 1/(2*\pi*R*C)$ (the equivalent circuit of the sensor is a high-pass filter). High leakage current and low capacitance result in a high cutoff frequency, which may cause distortion of the pulse wave signal (e.g., distortion of the relative positions of the systolic and diastolic peaks). In order to study the effect of the cutoff frequency of the e-tattoo sensor on the accuracy of the pulse wave, we fabricated three types of ferroelectric e-tattoo sensor samples with different bottom electrode materials (Ag, crosslinked PEDOT:PSS, and pristine PEDOT:PSS) resulting in varying leakage current and capacitance according to [2], and, hence, varying cutoff frequency (Table S3). The MCL was then used to generate a controlled pulse wave (at 50, 60, 70 and 80 BPM) to which the signal measured with the e-tattoo sensor was compared. The qualitative comparison of the generated and measured average amplitude-normalized pulse wave signals (see Figure 2 a to c for 60 BPM) reveals that the samples with low cutoff frequency (Figure 2a,b) produce an almost identical signal to the generated one, whereas the high cutoff frequency sample signal (Figure 2c) is heavily distorted. The most notable features are the time delay of the systolic and diastolic peaks (p_1 and p_2) and the attenuation of the diastolic peak. To quantify this difference, relative crest time ($RCT = tp_1/tp_t$; see Figure 2d for parameter definition), reflection index ($RI = p_2/p_1$), relative dicrotic wave time ($DWT = tp_2/tp_t$), and stiffness index ($SI = h/tp_2$, assuming h = 1.8m) pulse wave indices [19] were also extracted from both average signals, and their relative differences compared (see Table 2 for results at 60 BPM). The high cutoff frequency of the pristine PEDOT:PSS bottom electrode sample especially affects the RI, which quantifies the relative difference between the amplitudes of the systolic and diastolic peaks, and the RCT, which quantifies the relative difference between the time delay of these peaks. The Ag bottom electrode sample seems to produce a slightly better index correspondence when compared to the cross-linked PEDOT:PSS sample; however, this difference is likely related to variation in the measurement setup, as both samples have a low cutoff frequency smaller than the low cutoff frequency of the charge amplifier (~53mHz). Hence, it should be possible to use cross-linked PEDOT:PSS and Ag-bottom electrode samples interchangeably.

TABLE 2 | Absolute values of relative errors between the clinically relevant indices extracted from the pulse wave generated by the MCL, and pulse waves measured by e-tattoo sensors with Ag bottom electrode, cross-linked PEDOT:PSS electrode, and pristine PEDOT:PSS electrode at 60 BPM.

	Ag	Cross-linked PEDOT:PSS	Pristine PEDOT:PSS
ΔRCT (%)	0.2	4.8	56.3
ΔRI (%)	1.2	5.3	62.8
ΔSI (%)	1.1	1.9	30.2
ΔDWT (%)	1.6	1.9	23.2

3.2 | Improving Stretchability of the E-Tattoo Sensor for Integration to DTU

The DTUs consisted of a flexible PCB (containing, e.g., the optimized charge-amplifier for pulse-wave measurement) encapsulated in a soft elastomer, with the PCB-to-sensor connections located at one end of the DTU, the ferroelectric sensor element located at the opposite end of the structure, and a stretchable section in between (see Figure 3a).

In order to fully utilize the softness and stretchability of the DTU for improved user comfort, while simultaneously employing congruent fabrication methods, the e-tattoo sensor comprised inkjet-printed stretchable interconnects between the sensor element and the PCB-to-sensor connections (see Figure 3b). To this end, a horse-shoe geometry for the interconnect was adopted, and the stretchability was further enhanced by using an inkjet-printable, stretchable PEDOT:PSS solution (cross-linked PEDOT:PSS mixed with Glycerol), and by fabricating a stress-release pattern/layer from PDMS. Figure 3c shows the e-tattoo integrated on the DTU.

To more accurately simulate the stretching forces present when the DTU is attached to a wrist, an e-tattoo sensor with electrodes shorted through the P(VDF-TrFE) layer was integrated on the DTU. The change in resistance was measured using an electrometer while bending the DTU with a motorized tension/compression stand. The bending measurements were performed such that the e-tattoo sensor was either on the concave side (to simulate a measurement situation when the DTU is attached to the wrist) or the convex side of the bending (to simulate a more extreme bending situation, which could still

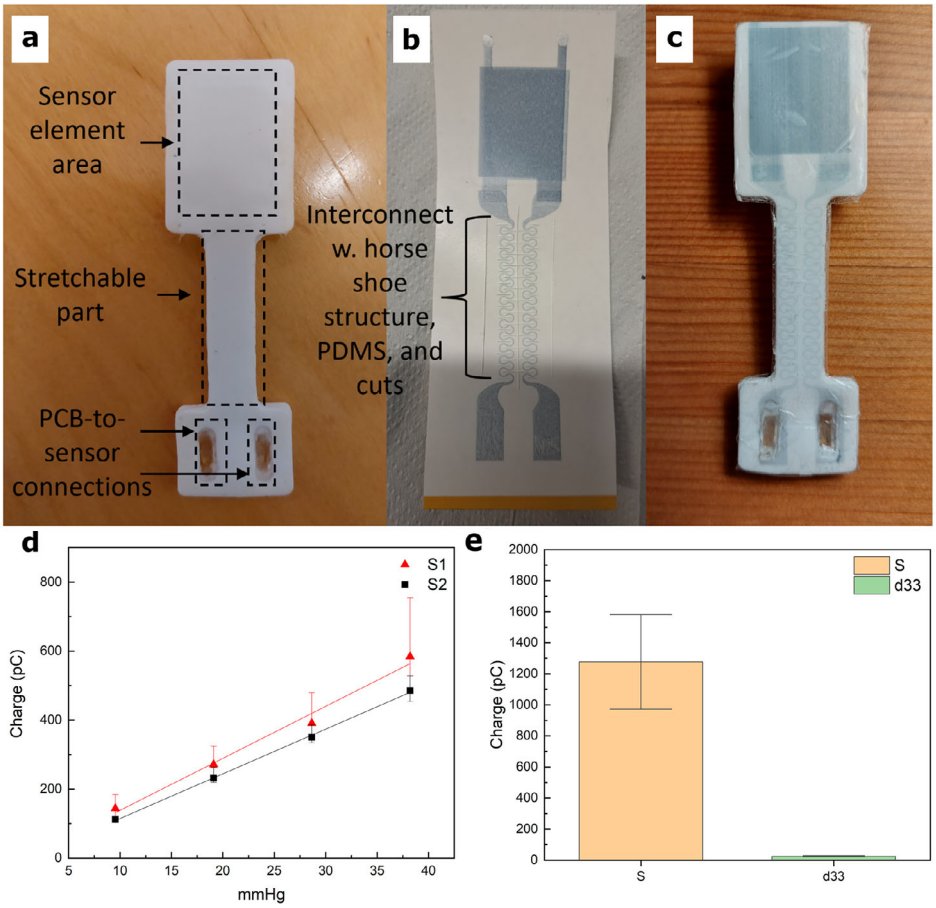

FIGURE 3 | a) Bottom view of the DTU, b) Ferroelectric e-tattoo sensor on temporary tattoo paper ready for integration into DTU, and c) Ferroelectric e-tattoo sensor integrated into DTU. d) Charge generated as a function of applied dynamic pressure in bending mode for two e-tattoo samples. Error bars show min-max values. Linear fit for S1: $R^2 = 98{,}68$, $\sigma = 32{,}2$ pC. Linear fit for S2: $R^2 = 99{,}90$, $\sigma = 7{,}7$ pC. e) Bar graph shows average bending mode sensitivity (S) of the two e-tattoo samples vs. the d33-coefficient for the same samples. Error bars show σ.

occur during handling of the device, Section S4). The movement distance was set to 10 mm, resulting in a bending radius of around 10 mm at maximum bending. Approximately 30 bending cycles were performed.

The development of resistance during ~30 concave bending cycles is shown in Figure S3 (Section S4). The resistance was normalized such that the starting value was 1. It is noteworthy that there is no sudden or significant increase in resistance, indicating that the conductors do not break during bending. It is also notable that the bending cycles themselves do not induce significant change in the resistance: Figure S3b for a zoomed-in view of resistance betweem10 to 40 s, and Figure S3c for the corresponding travel distance (z-axis in mm). However, the resistance steadily increases during the measurement, such that the final resistance after ~30 cycles is approximately twice the initial resistance (Figure S3a). This behavior is likely due to viscoelastic or plastic deformation of the conductors and/or the temporary tattoo material. From the perspective of the pulse-wave measurement, however, this increase should be negligible because the signal amplification is performed using a charge amplifier, which is insensitive to impedance changes in the load.

In addition to the bending tests, a separate resistance–strain measurement was performed to specifically investigate the maximum stretchability of the interconnection prior to electrical failure. The experimental setup and results are presented in the Supplementary Information (Section S4). These measurements show that the interconnection can accommodate strains of up to approximately 14%, exceeding the stretchability typically reported for pristine PEDOT:PSS conductors (≈5%) [20].

3.3 | Bending Mode Amplified Sensitivity

As shown in our previous paper [2], the sensitivity of the ferroelectric P(VDF-TrFE) based e-tattoo sensor can be significantly enhanced by placing it on a soft elastomeric material (such as the soft elastomer of the DTU), because the strain induced on the e-tattoo sensor is mainly determined by the strain induced on the soft elastomeric material. Since the quality of the pulse wave signal depends largely on the amplitude of the signal (i.e. on the signal-to-noise ratio), the bending mode enhanced sensitivity can be used to obtain a more accurate pulse wave signal. In our previous paper, the bending mode sensitivity S of the e-tattoo sensor was found to follow the relationship:

$$S = a * \frac{1}{E^b} + S_n$$

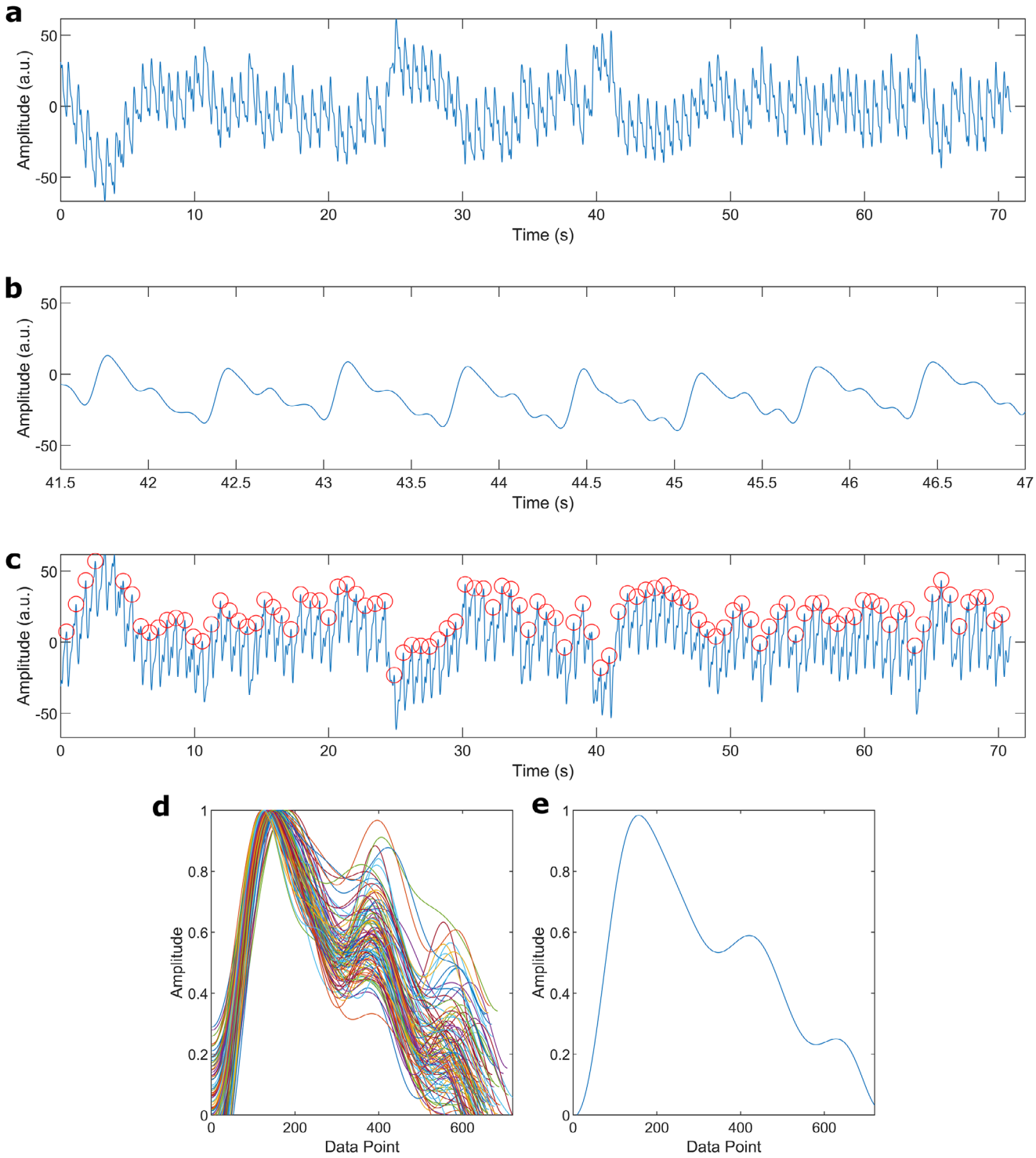

FIGURE 4 | a, b) Measured pulse waves after filtering, c) After pulse wave detection, wherein red circles indicate points used to separate the pulse wave signal into individual pulses, d) Overlaid individual pulses after amplitude normalization and trend-removal, and e) Average pulse wave calculated based on overlaid individual pulses.

where a and b are experimentally determined coefficients, E is the Young's modulus of the soft elastomer, and S_n is the sensitivity of the e-tattoo sensor when only compressive forces are present (i.e., normal mode sensitivity). The values of the parameters used in this estimation, including the Young's modulus, are provided in the Supplementary Information (Table S4). Using the coefficients from our earlier study, the measured d_{33}-coefficient as the value for S_n, and Young's modulus of the soft elastomer of the DTU, we can estimate that the sensitivity S of the e-tattoo sensor on DTU should be approximately 1360 pC N^{-1} on DTU.

To verify this estimate, d_{33}-coefficients of two e-tattoo sensors, fabricated with P(VDF-TrFE) cured at 120°C, were first measured while the e-tattoo sensors were still on the temporary tattoo

substrate. The same sensors were then integrated into the DTU, and their bending mode sensitivities were measured. The applied static and dynamic pressures were chosen to correspond to typical diastolic and systolic pressure, i.e., ~100 mmHg static pressure, and 9,6 mmHg to 38,2 mmHg dynamic pressure, respectively. The generated charge is shown in Figure 3d as a function of the applied dynamic pressure in a bending mode situation. The excellent linear fits (S1: $R^2 = 98{,}68$, $\sigma = 32{,}2$ pC; S2: $R^2 = 99{,}90$, $\sigma = 7{,}7$ pC) indicate linear sensor behavior within the dynamic range of a typical pulse wave signal, and, hence, negligible pulse wave signal distortion. A comparison of the average d_{33}-coefficient and bending mode sensitivity S of the e-tattoo sensors is shown in Figure 3e. As shown, the average bending mode sensitivity of 1277 pC N^{-1} for the e-tattoo sensors integrated on the DTU is approximately 50-times higher than the sensitivity of the same e-tattoo sensor in normal mode (25 pC N^{-1}). This sensitivity enhancement should translate directly to a higher S/N-ratio and, hence, to a more accurate pulse wave signal.

3.4 | Pulse Wave Measurement

The pulse wave signal was measured from a healthy 36-year-old male subject by pressing the developed wireless pulse wave measurement device against the radial artery at the wrist and recording the thus obtained pulse wave signal wirelessly on an iPad application (Figure S6 and Section S6 for a picture of the measurement setup). To analyze the obtained pulse wave, a second-order Butterworth filter with a passband of 50mHz to 7 Hz was used to reduce baseline wandering and eliminate high-frequency noise (e.g., 50 Hz mains interference). Figure 4 a shows the pulse wave signal after applying the Butterworth filter, and Figure 4b provides a zoomed-in view of the pulses. This was followed by detecting the individual pulses in the continuous pulse wave signal by first inverting the pulse wave signal and then separating the pulse wave signal into individual pulses based on data points detected by using a pre-determined peak prominence and peak-to-peak distance. Figure 4c shows the inverted pulse wave with detected individual pulses marked by red circles. Next, a linear trend was removed from the individual pulses based on the starting and ending points, followed by amplitude normalization of the individual pulses. The resulting individual normalized pulses are shown overlaid in Figure 4d. An average pulse waveform was then calculated based on the amplitude-normalized individual pulses (see Figure 4e), the total number of pulses included in the average was 108.

The following clinically relevant pulse indices were extracted from the amplitude normalized and averaged pulse shown in Figure 4e: relative crest time (RCT = TP1/TPT), reflection index (RI = AP2/AP1), relative dicrotic wave time (DWT = TP2/TPT) and stiffness index (SI = H/T2, where H is the height of the study subject in meters). Following are the results: RCT = 0.2, RI = 0.6, DWT = 0.6, SI = 6.8. The values correspond to typical values obtained for a healthy individual [21–23].

4 | Conclusion

In this study, we have developed a wireless and soft pulse wave measurement device with an integrated ferroelectric e-tattoo sensor. Specifically, we have optimized a printing-based fabrication process for a ferroelectric e-tattoo sensor for pulse wave measurement, showing that the e-tattoo sensor sensitivity can be improved in pulse wave measurement by integrating it into a soft elastomer-based wireless data transmission unit, and, finally, demonstrated the performance of the system in measuring radial arterial pulse wave at the wrist. Although the pulse-wave measurement demonstrates proof-of-concept functionality, the current validation is limited to a single subject. Future work should address system reliability by including tests on more participants as well as long-term stability and sensor–DTU connection reliability evaluations (e.g., 24-h drift tests) to further support practical deployment.

Author Contributions

Karem Lozano Montero. contributed to investigation, methodology, formal analysis, writing – original draft preparation, and writing – review and editing. **Yayun Du**. contributed to investigation and writing – original draft preparation, as well as writing – review and editing. **Ninja Kajas**. contributed to investigation and writing – review and editing. **Jacob Trueb**. contributed to software and writing – review and editing. **Mikko Peltokangas** and **Hany Arafa**. contributed to investigation and writing – review and editing. **Jin Tae Kim**. contributed to writing – review, and editing. **Jianyu Gu** and **Remmi Calvo Guzman**. contributed to the investigation. **Jiantong Li**. contributed to resources and writing – review and editing. **Niku Oksala** and **Antti Vehkaoja**. contributed to writing – review, and editing. **John Rogers** and **Matti Mäntysalo**. contributed to resources, supervision, and writing – review and editing. **Mika-Matti Laurila**. contributed to resources, investigation, conceptualization, methodology, formal analysis, writing – original draft preparation, writing – review and editing, and supervision.

Acknowledgments

K.L.M would like to thank Walter Ahlström Foundation and Tekniikan edistämissäätiö for support. The research used the Research Infrastructures "Printed Intelligence Infrastructure" (PII-FIRI, Academy of Finland Grant 320019). N. K. would like to thank Jane and the Aatos Erkko Foundation for support. M-M. L. would like to thank Walter Ahlström Foundation and Tutkijat Maailmalle program and acknowledge the financial support by H2020 Marie Skłodowska-Curie Actions (MSCA) Individual Fellowship (IF) Grant UNOPIEZO (Grant Number 10102243).

Open access publishing facilitated by Tampereen yliopisto ja Tampereen ammattikorkeakoulu, as part of the Wiley - FinELib agreement.

Funding

Tutkijat Maailmalle; Jane ja Aatos Erkon Säätiö; Tekniikan Edistämissäätiö; Walter Ahlströmin Säätiö; Academy of Finland 320019; HORIZON EUROPE Marie Sklodowska-Curie Actions 10102243.

Conflicts of Interest

The authors declare no conflicts of interest.

Data Availability Statement

The data that support the findings of this study are available from the corresponding author upon reasonable request.

References

1. H. Li, P. Tan, Y. Rao, et al., "E-Tattoos: Toward Functional but Imperceptible Interfacing with Human Skin," *Chemical Reviews* 124 (2024): 3220–3283.

2. M.-M. Laurila, M. Peltokangas, K. L. Montero, et al., "Self-Powered, High Sensitivity Printed e-Tattoo Sensor for Unobtrusive Arterial Pulse Wave Monitoring," *Nano Energy* 102 (2022): 107625.

3. K. L. Montero, M.-M. Laurila, M. Peltokangas, et al., "Self-Powered, Ultrathin, and Transparent Printed Pressure Sensor for Biosignal Monitoring," *ACS Applied Electronic Materials* 3 (2021): 4362–4375.

4. A. Petritz, E. Karner-Petritz, T. Uemura, et al., "Imperceptible Energy Harvesting Device and Biomedical Sensor Based on Ultraflexible Ferroelectric Transducers and Organic Diodes," *Nature Communications* 12 (2021): 2399.

5. D. Y. Park, D. J. Joe, D. H. Kim, et al., "Self-Powered Real-Time Arterial Pulse Monitoring Using Ultrathin Epidermal Piezoelectric Sensors," *Advanced Materials* 29 (2017): 1702308.

6. T. Sekine, R. Sugano, T. Tashiro, et al., "Fully Printed Wearable Vital Sensor for Human Pulse Rate Monitoring Using Ferroelectric Polymer," *Scientific Reports* 8 (2018): 4442.

7. C. Dagdeviren, Y. Su, P. Joe, et al., "Conformable Amplified Lead Zirconate Titanate Sensors with Enhanced Piezoelectric Response for Cutaneous Pressure Monitoring," *Nature Communications* 5 (2014): 4496.

8. C. Dagdeviren, Y. Shi, P. Joe, et al., "Conformal Piezoelectric Systems for Clinical and Experimental Characterization of Soft Tissue Biomechanics," *Nature Materials* 14 (2015): 728–736.

9. C. Dagdeviren, B. D. Yang, Y. Su, et al., "Conformal Piezoelectric Energy Harvesting and Storage From Motions of the Heart, Lung, and Diaphragm," *Proceedings of the National Academy of Sciences* 111 (2014): 1927–1932.

10. J. Kim, G. A. Salvatore, H. Araki, et al., "Battery-Free, Stretchable Optoelectronic Systems for Wireless Optical Characterization of the Skin," *Science Advances* 2 (2016): e1600418.

11. S. I. Zida, Y. Lin, and Y. L. Khung, "Current Trends on Surface Acoustic Wave Biosensors," *Advanced Materials Technologies* 6 (2021): 2001018.

12. X. Ye, L. Fang, B. Liang, et al., "Studies of a High-Sensitive Surface Acoustic Wave Sensor for Passive Wireless Blood Pressure Measurement," *Sensors and Actuators A: Physical* 169 (2011): 74–82.

13. R. Gregorio and M. M. Botta, "Effect of Crystallization Temperature on the Phase Transitions of P(VDF/TrFE) Copolymers," *Journal of Polymer Science Part B: Polymer Physics* 36 (1998): 403–414.

14. P.-H. Ducrot, I. Dufour, and C. Ayela, "Optimization of PVDF-TrFE Processing Conditions for the Fabrication of Organic MEMS Resonators," *Scientific Reports* 6 (2016): 19426.

15. Arkema Piezotech Datasheet, (n.d.).

16. G. Hernandez-Cuevas, J. R. Leyva Mendoza, P. E. García-Casillas, et al., "Effect of the Sintering Technique on the Ferroelectric and d_{33} Piezoelectric Coefficients of $Bi_{0.5}(Na_{0.84}K_{0.16})_{0.5}TiO_3$ Ceramic," *Journal of Advanced Ceramics* 8 (2019): 278–288.

17. S. Millasseau, "The Vascular Impact of Aging Andvasoactive Drugs: Comparison of Twodigital Volume Pulse Measurements," *American Journal of Hypertension* 16 (2003): 467–472.

18. M. Peltokangas, A. Vehkaoja, J. Verho, M. Huotari, J. Roning, and J. Lekkala, "Monitoring Arterial Pulse Waves with Synchronous Body Sensor Network," *IEEE Journal of Biomedical and Health Informatics* 18 (2014): 1781–1787.

19. M. F. O'Rourke, A. Pauca, and X. Jiang, "Pulse Wave Analysis," *British Journal of Clinical Pharmacology* 51 (2001): 507.

20. Y. Wang, C. Zhu, R. Pfattner, et al., "A Highly Stretchable, Transparent, and Conductive Polymer," *Science Advances* 3 (2017): e1602076.

21. J. Nürnberger, S. Dammer, A. Opazo Saez, T. Philipp, and R. F. Schäfers, "Diastolic Blood Pressure is an Important Determinant of Augmentation Index and Pulse Wave Velocity in Young, Healthy Males," *Journal of Human Hypertension* 17 (2003): 153–158.

22. A. Wykretowicz, K. Adamska, P. Guzik, T. Krauze, and H. Wysocki, "Indices of Vascular Stiffness and Wave Reflection in Relation to Body Mass Index or Body Fat in Healthy Subjects," *Clinical and Experimental Pharmacology and Physiology* 34 (2007): 1005–1009.

23. J. Nürnberger, A. Keflioglu-Scheiber, A. M. Opazo Saez, R. R. Wenzel, T. Philipp, and R. F. Schäfers, "Augmentation Index is Associated with Cardiovascular Risk," *Journal of Hypertension* 20 (2002): 2407–2414.

Supporting Information

Additional supporting information can be found online in the Supporting Information section.

Supporting File: adsr70135-sup-0001-SuppMat.pdf

Supporting File: adsr70135-sup-0002-MovieS1.mp4